Influence of Pulse Repetition Rate on Morphology and Material Removal Rate of Ultrafast Laser Ablated Metallic Surfaces

X. Sedao[a,b], M. Lenci[c], A. Rudenko[a], N. Faure[a], A. Pascale-Hamri[b], JP. Colombier[a], C. Mauclair[a,b,*]

[a] *Laboratoire Hubert Curien, UMR 5516 CNRS, Université de Lyon, Université Jean Monnet, Institute of Optics Graduate School, 42000 Saint-Etienne, France*
[b] *GIE Manutech-USD, 42000 Saint-Etienne, France*
[c] *Mines Saint-Etienne, Univ Lyon, CNRS, UMR 5307 LGF, Centre SMS, F - 42023 Saint-Etienne France*

Abstract

Ultrafast laser ablation is an efficient method for precise micro-machining. Thanks to the recent development of high repetition rate ultrafast lasers, high speed laser scanning of surfaces is more and more employed to generate micro-/nano-surface structures on metals for a vast variety of applications. Issues associated with these lasers are also identified in micro-machining practice. It is commonly believed that, due to possible shielding effects, the conditions of high fluences and high repetition rates compromise an efficient material removal. However, in this study, based on topography and differential weighing evaluations, we report that the material removal rate holds constant even in sub-MHz regime, up to about 20 J/cm^2. The morphology of the post-irradiated surface is found to be determined not only by laser processing conditions but also by the material properties on the other hand. Two trends are experimentally identified in surface laser ablation of Ni, Cu, titanium alloy TA6V and stainless steel 316L: while the former two show a low roughness (Ra below 0.5μm) at all irradiation conditions, the machining quality of the two later ones degrades rapidly with increasing fluences and repetition rates. In such a scenario, a rugged surface

*Corresponding author
Email address: cyril.mauclair@univ-st-etienne.fr (C. Mauclair)

layer of 10-20μm thickness is formed with the presence of numerous subsurface voids. Microstructural analysis is carried out in order to infer physical transition involved in the micro-machining process. Possible mechanisms accounting for the observation are discussed, especially those related to the electron-phonon coupling, plasma dwelling, and capillary waves. These insights pave the way for tailored, material dependent optimizations of ultrafast laser micro-machining processes.

Keywords: ultrafast laser ablation, fluence, repetition rate, removal rate, surface roughness, heat accumulation.

---

1. Introduction

Ultrashort pulse laser ablation of metals has been investigated extensively for decades and successful applications have been demonstrated in vast fields including surgery, biology, tribology, wettability, color marking and cutting [1, 2, 3, 4, 5, 6, 7, 8, 9]. A metal surface irradiated by an intense femtosecond laser pulse experiences rapid heating of its electronic system and undergoes phase explosion of the superheated melt layer [10, 11, 12]. The ablation takes place including ejection of nano-particles and leaves behind a minimum heat-affected zone. Therefore, material removal by femtosecond laser pulse ablation is characterized by an ultimate high precision. The rapid advances in laser technology make high-performance ultrashort pulse lasers readily available on the market, with pulse repetition rate up to MHz and a few hundreds Watts output power [13]. This technology boom undoubtedly opens up more ultrashort laser processing potentials and boosts up existing applications. However, new issues associated particularly with high fluence and repetition rate limit the potentialities of ultrafast laser ablation. For instance, particle shielding and heat accumulation were found to have significant influence on the ablation in this regime, negating the machining efficiency and quality, respectively [14, 15, 16, 17, 18, 19, 20]. Weber demonstrated numerically that in percussion drilling CrNi-steel scenario the residual heat accumulation is more pronounced

at high repetition rate of 250 kHz than at lower one of 50 kHz [15]. Although such thermal effect along with particle shielding should be supposedly mitigated by raster scanning of the laser beam over a large surface and supporting experimental results are obtained from Cu micro-machining [21], seemingly controversial adverse impacts on ablation quality of stainless steel have also been reported in literature and the cause was attributed to a substrate temperature related empirical factor [14]. It is obvious that the accumulative heat effect, particle shielding effect, and possibly other role-playing effects, are dependent on both laser processing conditions and certain thermal properties of the targeted metal, therefore a comparative study on micro-machining of typical metals should shed lights on the underlying issues.

In the present work we investigate the influence of laser fluence and repetition rate on micro-machining by raster scanning of several commonly used industrial metals/alloys. The material removal rate and the resulting surface topography are thoroughly characterized. Based on the micro-machining quality, these metals/alloys can be categorized into two groups: one group can be micro-machined under the combination of high fluence and repetition rate without undermining the quality degradation, while greater care has to be given to the other group as the machining quality of these materials degrades markedly at aforesaid laser processing conditions. Microstructural analysis and review of the material properties are also employed in this study to help interpret the observations.

2. Experimental and calculation details

The experimental study is focused on the ablation rate and surface geometry development upon laser irradiation at different fluence and at different repetition rate. A schematic drawing of the laser setup and raster scan strategy is depicted in Fig. 1(a). The materials of interest are commonly used engineering/industrial metals and alloys, including Ni, Cu, titanium alloy TA6V and stainless steel 316L. The targets were prepared by conventional metallography procedures with

a final surface roughness average Ra = 20 nm. The micro-machining was carried out using a fiber fs laser system (Tangerine HP of Amplitude Laser Group). The laser has a central wavelength of 1030 nm with a pulse duration of 350 fs at full width half maximum and a repetition rate (R) tunable from single shot to 2 MHz. The linearly polarized laser pulses were attenuated, sent through a galvano scanner and focused through a 100 mm telecentric f-theta lens. The focused laser spot exhibits a Gaussian profile and the spot diameter (at $1/e^2$) measures $2\omega_0 = 22\,\mu$m. For micro-machining a surface area, a raster scanning strategy was used. The overlap ratio of 0.91 between successive laser pulses and between successive laser scan tracks was kept constant for all the experiments and all the materials. The laser fluence quoted in this paper is the peak fluence $F = 2\varepsilon/\pi\omega_0^2$, with ε being the laser pulse energy. The laser fluence variation window was 0.6 - 18 J/cm^2, from just above to a few tens of times of the ablation threshold for the materials. The repetition rate was varied between 31 kHz and 500 kHz. The lower bond of the repetition rate was set on a value below which the machining throughput would be no longer of interest from an industrial processing point of view. The upper value was set based on a joint consideration of maximum available laser pulse energy and scanner speed limit.

The topographical analysis of surface modifications in the laser impacted area was performed using a chromatic confocal microscope (Stil). A 3-dimensional representation given in Fig 1(b) is re-constructed surface topography of the laser micro-machined trenches. The ablation volume and surface roughness of laser irradiated areas were derived from topographical analysis. As reported later in this study, certain laser processing conditions may cause the formation of deep micro-holes and/or enclosed cavities to form on the irradiated surface, the depth of which is no longer measurable by the confocal microscope. In such case, the ablation rate was evaluated using a differential weighing method, which was based on a mass measurement of ablated material. The sample is weighed before and after machining [22]. The difference in the sample mass corresponds to the mass of ablated material. The micro-balance is of model XP26 from Mettler-Toledo. In order to inspect the surface morphology and the microstruc-

ture beneath the surface, some selected areas were analyzed with a dual beam SEM/FIB. Two types of analyzes are presented in this paper: the SEM observations on the surface after laser irradiation; and FIB cross sections on ablated areas in order to observe the microstructure evolution in the longitudinal direction (from the irradiated surface down to the bulk). The aforementioned analyzes were achieved on a FEI Helios Nanolab 600i dualbeam workstation. An example of surface and cross-section inspections by SEM/FIB is presented in Fig. 1(c).

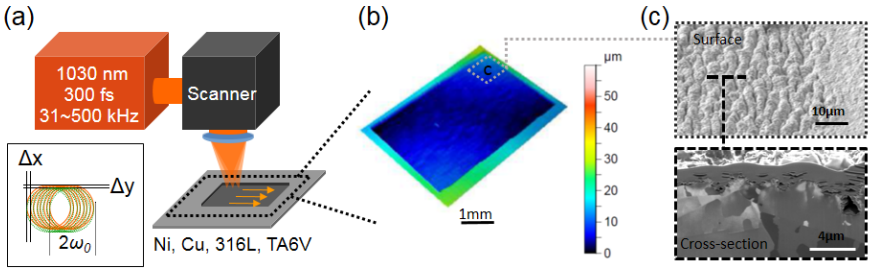

Figure 1: Sketch of the experimental procedure: (a) Each sample was irradiated with the same total number of laser pulses following the illustrated scan path with $\Delta x=\Delta y=2\mu m$, and $2\omega_0$ being the spot diameter at $1/e^2$. (b) Surface topography analysis was carried out using a confocal microscope, and ablation rate was evaluated based upon the topographical measurement. In addition, differential weighing before and after laser irradiation was also carried out to access ablation rate in certain circumstances. (c) SEM-based imaging techniques were performed for surface morphology (upper image) and FIB-prepared cross-section inspections (lower image). The bold dashed line in the upper image indicates where the cross-section was to be made, and the lower image shows the FIB-prepared cross-section.

3. Results and discussion

The ablation rate is evaluated in the form of ablation volume per laser pulse. The surface finishing quality is characterized by surface roughness essentially extracted from surface topography measurement. The four materials investigated

in the present work, according to their evaluation characteristics, can be divided into two categories, the first including Ni and Cu, and the second being stainless steel 316L and TA6V.

A typical panel of Ni micro-machining evaluation, following above-mentioned criteria, is represented in Fig. 2, where the material removal rate, surface roughness, morphology and topography are given. The material ablation is plotted against laser fluence and repetition rate in Fig. 2(a). As expected, at any given repetition rate, the higher the laser fluence, the greater the removal rate. The plot is based on confocal surface topography measurement. The tendency shown in Fig. 2(a) is also cross checked using the data from the differential weighing based mass change measurement, as well as existing data from the literature (with presumably negligible differences in terms of pulse duration 120 fs, wavelength 800 nm and repetition rate 5 kHz) [23]. Across the entire range of repetition rate tested, the removal rate appears to be fairly constant. This near-constant ablation removal rate agrees well with high repetition rate fs laser drilling reported in literature [24]. The ablation removal rate only slightly increases at higher repetition rate observed for high laser fluence, i.e. 18 J/cm^2. Regarding the surface finishing of laser machined Ni surface, Fig.2(b) depicts the correlation between surface roughness Ra and the laser conditions employed to produce these surfaces. It is clear that the resulting Ra remains remarkably low, even at high fluence and high repetition rate. The SEM image (Fig. 2(c)) shows the homogeneous morphology attained at the center of the laser-irradiated surface. The reconstructed surface topography at the border area of the laser machined surface, shown in Fig. 2(d), also reveals a homogeneous surface finishing from a 3-dimensional perspective. All these facts suggest an excellent machinability of Ni. For industrial processing purposes, where the machining throughput is demanding, the high power and high repetition rate of modern femtosecond lasers can be fully exploited.

An analogy in terms of machinability is drawn between Ni and Cu. For the sake of simplicity while being informative, only the removal rate and surface roughness are plotted against the laser conditions and given in Fig. 3.

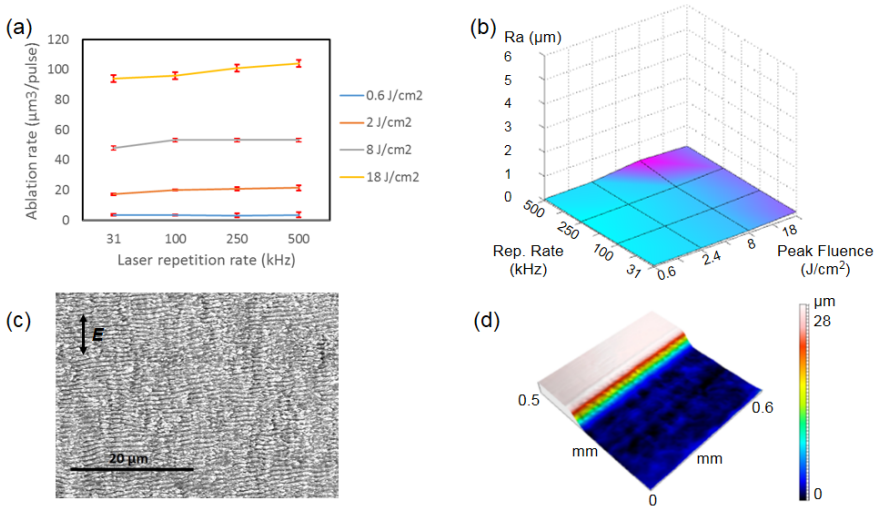

Figure 2: Near constant ablation rate at any repetition rate, and all over low surface roughness for nickel micro-machining. (a) Removal rate per laser pulse; (b) Surface roughness Ra is plotted against laser repetition rate and laser fluence; (c) A SEM micrograph showing the typical surface finishing of micro-machined Ni. The black arrow indicates the laser polarization; and (d) reconstructed 3-dimensional surface topography illustrates good quality and fast ablation achievable even at high fluence and repetition rate. The process conditions in (c) and (d) are F= 18 J/cm^2 and R = 500 kHz.

Fig. 4 shows the evaluation panel for stainless steel 316L from the second group. A marked departure from Ni and Cu, especially pronounced in high fluence and high repetition rate regime, is captured by the confocal probe based measurements, i.e. the removal rate derived from topography in Fig. 4(a) (solid lines), and surface roughness evolution (Fig. 4(b)). The ablation removal rate is plotted in the same fashion in Fig. 4(a) as in Fig. 2 and 3. As far as degraded surface topography is concerned, confocal microscope based approach fails to deduce a reliable material removal rate, because of geometrical confinement to the probing light at such surfaces (dedicated geometry study will be given in the later section). This is the reason why one observes a forward-falling curve with repetition rate, at 8 J/cm^2 in the removal rate plot (solid lines). For the sake of clarity and readability of the plot, the material removal rate data

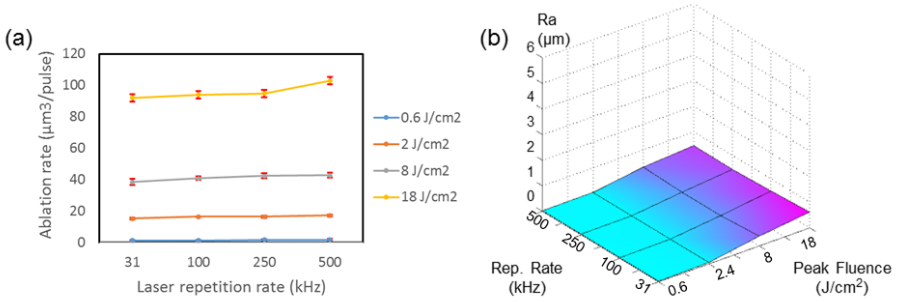

Figure 3: Ablation rate and micro-machining quality of copper are comparable to those of nickel. (a) Removal rate per laser pulse of copper; (b) surface roughness Ra is plotted against laser repetition rate and laser fluence.

points from the confocal microscope-based approach at high fluence and repetition rate are left out, namely, those for 8 J/cm^2 at 500 kHz, 18 J/cm^2 at 250 and 500 kHz. The accurate removal rates at these conditions are derived from the more direct differential weighing based approach (dashed lines). Strikingly, the ablation rates at 250 kHz and 500 kHz, notwithstanding the rugged surface appearance, remain the same as those at 31 kHz and 100 kHz. Overall, the removal rate for 316L, alike those for Ni and Cu, is only dependent on fluence but independent on the repetition rate in the investigated parameter range between 31 and 500 kHz, despite the sharp contrast in morphology and topography of the micro-machined surfaces at low and high repetition rates. Higher repetition rates (typically from the MHz to a few tens of MHz) are accompanied by interaction phenomena that can be detrimental for surface scanning ablation quality, such as heat accumulation [15, 19], and particle ejection and shielding observed on the μs timescale [25]. Noteworthy, this corresponds to the MHz repetition rate limit. The surface roughness of micro-machined surfaces is plotted in Fig. 4(b). Compared to the Ra values of micro-machined Ni and Cu, the surface roughness of 316L is obviously more sensitive to laser processing parameters, the fluence and repetition rate. At 31 and 100 kHz, the micro-machined surface remains smooth for all fluences used in this study (Fig. 4(b)). A sharp transi-

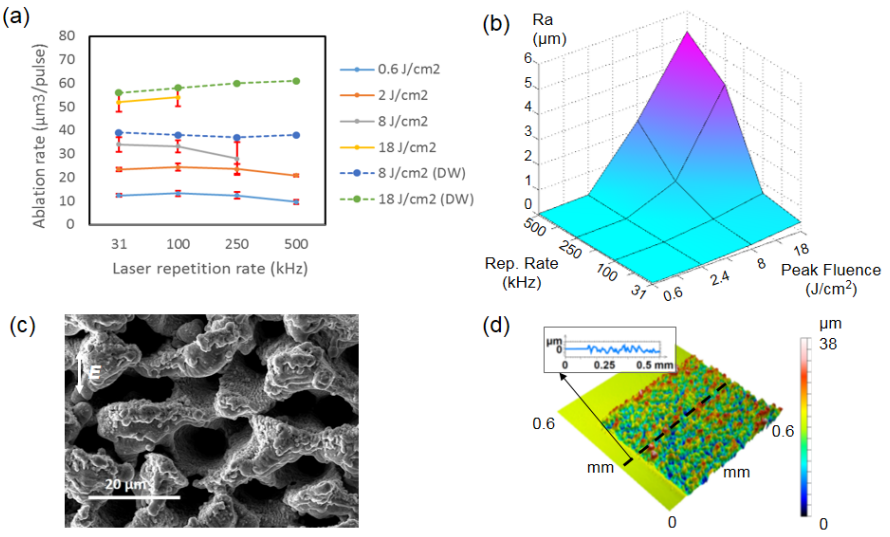

Figure 4: Removal rate per laser pulse on stainless steel 316L (a) differential weighing (DW, dotted lines) based evaluation also presented to indicate ablation rate, in certain conditions where the confocal microscope based approach failed to yield reliable information; surface roughness Ra is plotted against laser repetition rate and laser fluence (b); A SEM micrograph in (c) showing rugged surface morphology obtained at high repetition rate (8 J/cm^2, 500 kHz). The white arrow points out the laser polarization; and (d) corresponding 3D surface profile depicting the topography, the inset on the upper corner showing an extracted 2D profile, demonstrating partial laser machined surface raised above the initial surface level.

tion is observed at higher repetition rates. An up to 10 to 20 folds greater Ra is observed for 316L than that for Ni and Cu, when the combination of high fluence and high repetition rate is applied. For many micro-machining applications, this could be a strong drawback and should be avoided. A representative SEM image taken from the surface irradiated at 8 J/cm^2 and 500 kHz reveals the rugged nature of the resulting morphology (Fig. 4(c)). A 3D topography of the irradiated surface and its vicinity is reconstructed in Fig.4(d). The inset is an extracted 2D profile right across micro-machined and un-irradiated surface. The bumpy nature of this micro-machined surface is evident, with many hillocks rising beyond the initial surface level. Analogous morphologies are produced typically at high fluence and repetition rate, namely, 8 J/cm^2 at 250 kHz

and beyond.

The removal rate and surface roughness of titanium alloy TA6V machining are summarized in Fig. 5(a) and 5(b), respectively. TA6V exhibits a similar behavior to 316L. Regardless of repetition rate applied and resulting surface topology, at a given fluence, the removal rate is constant. Compared to 316L, TA6V is little less sensitive to repetition rate, and the process window is slightly extended to medium fluence, up until 8 J/cm^2. Beyond this value, the surface finishing degrades rapidly.

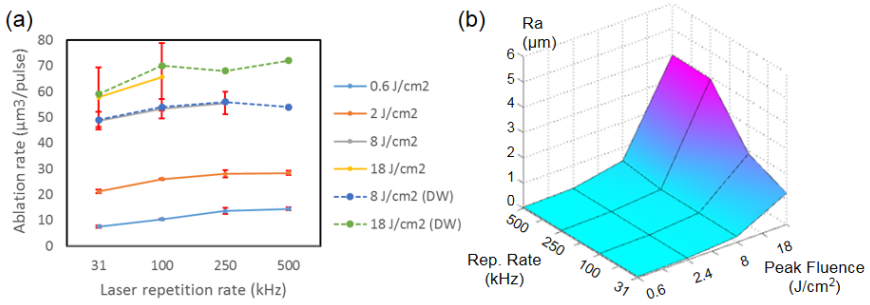

Figure 5: Removal rate per laser pulse of titanium alloy TA6V (a) differential weighing (DW, dotted lines) based evaluation also presented to indicate ablation rate, in certain conditions where the confocal microscope based approach failed to yield reliable information; surface roughness Ra is plotted against laser repetition rate and laser fluence (b).

The observation of constant material removal rate but significantly degraded surface morphology, sometimes with surface profile rising beyond the initial surface at high fluence and high repetition rate regime (for instance, see Fig. 4(a), 4(b) and 4(d)), is somewhat counterintuitive. In order to illustrate the topography transition to a greater extent, a schematic is drawn in Fig. 6(a). The illustration depicts the key disparity of surface finishing achieved at different processing conditions, and it is further elaborated by cross-sections extracted from such surfaces shown in Fig. 6(b). The SEM micrographs in Fig. 6(b) are from stainless steel 316L. Similar morphological and cross-sectional analysis has been done with titanium alloy TA6V, and similar behaviors are observed

(therefore the results from TA6V are not shown here). The surface micro-machined at 31 kHz falls below the initial surface level, and is featured by grooves with peak-to-valley amplitude typically smaller than 5 μm, as is shown in Fig. 6(b), left column, and Fig. 6(c). On the other side, the surface made at 500 kHz is full of hillocks with dimensions ranging 15 to 30 μm, the contour of micro-machined surface alternates between above and under the initial surface level. The hillocks are relatively sparse and μm-sized valleys may hide under the hillocks, as is unveiled from the cross-section image, shown in Fig. 6(b) right column, or Fig. 6(d). Since these images are of the same magnifications (for the purpose of comparison), the difference in topography development on the two surfaces manifests itself unarguably. The surface machined at 500 kHz is evidently more rugged and porous. Attempt has been made to evaluate the size and distribution of the valleys lodged between the hillocks. By FIB milling on the cross-section face continuously, the volume evolution was characterized and some of the valleys were indeed proved to be voids or cavities. In order to visualize these, a standing cross-section was made by FIB milling from the foreside and the backside of the selected site (see Fig. 6(d)). Hollows of roughly circular-shape of 5-10 μm in dimension are seen about 10 μm underneath the surface. Some voids of this sort can be seen in Fig. 6(d).

Metallurgical investigations were also pursued. The grain contrast micrographs of cross-sections sampled from 31 kHz and 500 kHz micro-machined surfaces are displayed in Fig. 6(c) and 6(d). Owing to the strong channeling effect of the chosen imaging mode, the crystal grains with different orientations differentiate themselves by the contrast. It is visible from Fig. 6(c) that the size of the grains in the contour region of the surface undulation, of approximately 5 μm thick, is smaller than the size of the grains in the bulk region underneath the undulations, suggesting grain regrowth associated with melting and re-solidification in the skin region of the surface undulation. Similarly, small grains are also identified within the hillocks. However, compared to 31 kHz case, the distribution of small sized grains at 500 kHz is much broader, occupying at least 10 to 15 μm surface region, from the top of the hillocks down into

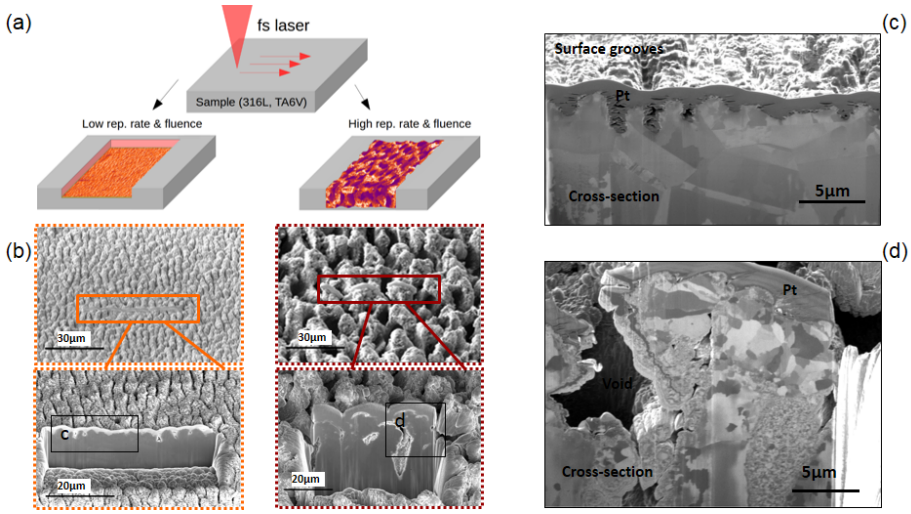

Figure 6: (a) Schematic illustration of different surface topography developments at a given laser fluence (8 J/cm^2) while different repetition rates (31 and 500 kHz). (b) Underneath the schematic drawings, the SEM images of stainless steel 316L samples micro-machined at the two repetition rates, providing more detailed supporting information. The color boxed areas from the upper surface SEM micrographs are the sites chosen for cross-section investigation. The cross-sections are shown underneath the surface SEM images. The boxes c and d in the cross-section images are chosen for FIB fine polishing and further illustrated in (c) and (d); (c) The grain structure revealed from the cross-section (8 J/cm^2, 31 kHz) after FIB etching and polishing suggests a melting - re-solidification transition in the groove region, within a few μm surface zone; (d) The grains structure (8 J/cm^2, 500 kHz) suggests a melting - re-solidification transition in the entire spikes region, of a few 10 μm surface zone. Pt denotes the Platinum protective layer necessary to the FIB etching process.

the bulk. Furthermore, at the edge of the hillocks, including the hollow region located between the two hillocks in Fig. 6(d), the grains are significantly smaller than the grains inside the hillocks. This might suggest that the formation of the central and skin parts of the hillocks did not occur at the same moment of the micro-machining, and/or the cooling speeds for the two counterparts were different. A complex interplay may be involved for the formation of such a microstructure. The bumpy surface finishing may be regarded as undesirable from standard view. Nevertheless, the porous status and increased roughness Ra may render the surface a superhydrophobic nature, thereby becoming appealing in

certain wetting applications [26, 4].

To explain the observed difference for various metals after multipulse high-intensity laser ablation, we analyze the material properties for the metals under investigation summarized in Table 1. The properties of titanium alloy TA6V are not well-known, therefore, we use here the properties of pure Ti. The striking difference is evident by comparing electron-phonon coupling constants γ and thermal conductivities K_i of these metals. The electron-ion transfer occurs significantly faster for stainless steel and Ti than for Ni and Cu, whereas the thermal conductivity of stainless steel and Ti is more than twice smaller than that of Ni and Cu. The electron-phonon coupling constant γ as well as the other material properties are used to calculate the heat penetration depth for different metals as follows $x = \sqrt[8]{\frac{128}{\pi}} \left(\frac{K_e^2 T_e C_i \rho}{T_m \gamma^2 C_e} \right)^{1/4}$ [27], where C_e and K_e are the electron heat capacity and conductivity, T_e is the electron temperature, T_m is the melting temperature, and C_i is the material heat capacity. The results are indicated in Table 1. The heat penetration depths are found to be greater for Ni and Cu than for Ti and stainless steel. This result indicates that the thermal energy is stronger confined on the surface of Ti and stainless steel. Additionally, more energy is absorbed on Ti and stainless steel surfaces for the same laser fluence, due to larger absorbance coefficients A (see Table 1). Both of these facts stand for higher surface temperatures and hotter laser-induced plasmas. The plasma can still remain on the surface for hundreds of nanoseconds, heating and explosively remelting the surface [28]. If we take account the fact that the cooling of Ti and stainless steel takes longer time than for Ni and Cu due to both lower thermal conductivities and hotter laser-induced plasma, we come to the conclusion that Ti and stainless steel should be more sensible to higher repetition rates. The ablation in this case typically leads to larger amount of surface roughness [29].

Another interesting observation is related to the formation of micrometer spikes after multipulse laser irradiation. Here, we verify the scenario of capillary wave role in spikes formation by making estimations of liquid lifetime defined as $\tau_l = \frac{\rho C_i x^2}{2K_i}$, the characteristic time of capillary wave establishment $\tau_{cw1} =$

$\frac{\lambda^2}{2\pi}\sqrt{\frac{\rho}{\sigma x}}$, where $\lambda \approx 2\mu m$ is the capillary wavelength corresponding to the typical size of formed spikes, ρ is the liquid density, and σ is the surface tension, and the characteristic period of capillary wave defined as $\tau_{cw2} = \frac{\rho\lambda^2}{8\pi^2\nu}$, where ν is viscosity [30]. The used values for different metals, as well as the results, are indicated in Table 1. According to the estimations, the characteristic times τ_{cw1} and τ_{cw2} are much longer than the liquid lifetime, which is of order of few nanoseconds for Ni and less than nanosecond for other metals. The additional heating of the surface melt layer by laser-induced plasma, however, is not taken into account by the simple expression. Nevertheless, an argument can be drawn upon, independent of the estimated liquid lifetime, is that the conditions for spike formation by capillary wave $\tau_{cw1} < \tau_{cw2}$ are satisfied only for Ni. Spikes, however, have been observed as well for titanium alloy TA6V and stainless steel 316L experimentally, which implies that other physical phenomena are involved in spike formation, such as pulse overlapping, plasma-induced surface debris or thermo-fluidic effects arising by thermal accumulation [31, 32].

4. Conclusion

We investigated the machinability of a few technologically important metals and alloys, including Ni, Cu, titanium alloy TA6V, and stainless steel 316L, in a wide range of laser fluences and repetition rates, namely 0.6-18 J/cm^2 and 31-500 kHz. The material removal rate and surface finishing were evaluated. The removal rate for all the materials is shown to be dependent on laser fluence, but independent on repetition rate. Concerning surface finishing, Ni and Cu appear to withstand harsh conditions: low surface roughness (Ra $<$ 500 nm) can be achieved, even at the combination of high fluence and high repetition rate. TA6V and 316L are, on the contrary, found to be more sensitive to laser processing conditions. Even at medium laser fluence of 8 J/cm^2, the surface roughness degrades rapidly with increasing repetition rate. Micro-structural analysis revealed that under high fluence conditions, a surface layer experiencing melting and re-solidification transitions is manifested by the presence of overall

Table 1: Material properties of metals.

Physical properties	Ni	Cu	Ti	Steel
Absorbance A [33]	0.26	0.04	0.38	0.44
E-ph coupling constant $\gamma[10^{17}\,\mathrm{Wm^{-3}K^{-1}}]$ at $2\cdot10^4$K [34, 35]	1.11	6.46	27.69	31.7
Electron thermal conductivity $K_e[\mathrm{Wm^{-1}K^{-1}}]$ at $2\cdot10^4$K [35, 36]	1600	1000	1000	1070
Electron heat capacity $C_e[10^5\,\mathrm{Jm^{-3}K^{-1}}]$ at $2\cdot10^4$K [34, 35]	32.4	38.9	20.3	33.8
Melting temperature T_m [K] [37]	1727	1356	1958	1809
Liquid density $\rho[\mathrm{g\cdot cm^{-3}}]$ at T_m [37]	7.905	8.0	4.11	6.881
Viscosity $\nu[10^{-3}\mathrm{Pa\cdot s}]$ at T_m [37]	4.6	4.1	5.2	8.0
Thermal conductivity K_i $[\mathrm{Wm^{-1}K^{-1}}]$ at T_m [37]	60	163	31	29
Heat capacity C_i $[\mathrm{J\cdot g^{-1}K^{-1}}]$ at T_m [37]	0.657	0.494	0.966	0.79
Surface tension σ [N/m] at T_m [38]	1.78	1.29	1.65	1.87
Heat penetration depth x [nm]	396	123	64	60
Liquid lifetime τ_L [ns]	6.79	0.183	0.262	0.255
Capillary wave establishment τ_{cw1} [ns] for $\lambda = 2\mu$m	67	143	125	157
Capillary wave period τ_{cw2} [ns] for $\lambda = 2\mu$m	86.9	99.0	40.1	43.6

small grain components inside this layer. At low repetition rate, this layer occupies merely a thin surface region. At high repetition conditions, this re-solidified layer forms a some 20 μm thick porous and rugged surface region. Therefore, for these materials, special attention should be drawn in the micro-machining practices. Amongst other physical properties, the electron-phonon coupling constant and thermal conductivity of the materials in question are considered to be responsible for the difference observed experimentally.

5. Acknowledgements

The authors thank French ANR for the Equipex MANUTECH-USD support (Investissements d'Avenir ANR-10-EQPX-36-01). This work was carried out for LABEX MANUTECH-SISE financed project ICRAM. This work was also supported by the IMOTEP project within the program Investissements dAvenir operated by ADEME.

References

[1] V. Dumas, A. Guignandon, L. Vico, C. Mauclair, X. Zapata, M. T. Linossier, W. Bouleftour, J. Granier, S. Peyroche, J.-C. Dumas, H. Zahouani, Aline Rattner, Femtosecond laser nano/micro patterning of titanium influences mesenchymal stem cell adhesion and commitment, Biomedical Materials 10 (5) (2015) 055002. doi:10.1088/1748-6041/10/5/055002.

[2] C. Jumelle, A. Hamri, G. Egaud, C. Mauclair, S. Reynaud, V. Dumas, S. Pereira, T. Garcin, P. Gain, G. Thuret, Comparison of four methods of surface roughness assessment of corneal stromal bed after lamellar cutting, Biomedical Optics Express 8 (11) (2017) 4974–4986. doi:10.1364/BOE.8.004974.

[3] J. Dufils, F. Faverjon, C. Heau, C. Donnet, S. Benayoun, S. Valette, Combination of laser surface texturing and DLC coating on PEEK for enhanced tribological properties, Surface and Coatings Technology 329 (Supplement C) (2017) 29–41. doi:10.1016/j.surfcoat.2017.09.028.

[4] O. Raimbault, S. Benayoun, K. Anselme, C. Mauclair, T. Bourgade, A.-M. Kietzig, P.-L. Girard-Lauriault, S. Valette, C. Donnet, The effects of femtosecond laser-textured Ti-6al-4v on wettability and cell response, Materials Science and Engineering: C 69 (Supplement C) (2016) 311–320. doi:10.1016/j.msec.2016.06.072.

[5] B. Dusser, Z. Sagan, H. Soder, N. Faure, J. P. Colombier, M. Jourlin, E. Audouard, Controlled nanostructrures formation by ultra fast laser pulses for color marking, Optics Express 18 (3) (2010) 2913–2924. doi:10.1364/OE.18.002913.

[6] Z. Liu, J. Siegel, M. Garcia-Lechuga, T. Epicier, Y. Lefkir, S. Reynaud, M. Bugnet, F. Vocanson, J. Solis, G. Vitrant, N. Destouches, Three-Dimensional Self-Organization in Nanocomposite Layered Systems by Ultrafast Laser Pulses, ACS Nano 11 (5) (2017) 5031–5040. doi:10.1021/acsnano.7b01748.

[7] C. Mauclair, D. Pietroy, Y. Di Maio, E. Baubeau, J.-P. Colombier, R. Stoian, F. Pigeon, Ultrafast laser micro-cutting of stainless steel and PZT using a modulated line of multiple foci formed by spatial beam shaping, Optics and Lasers in Engineering 67 (Supplement C) (2015) 212–217. doi:10.1016/j.optlaseng.2014.11.018.

[8] J. Bonse, S. V. Kirner, R. Koter, S. Pentzien, D. Spaltmann, J. Krger, Femtosecond laser-induced periodic surface structures on titanium nitride coatings for tribological applications, Applied Surface Science 418 (Part B) (2017) 572–579. doi:10.1016/j.apsusc.2016.10.132.

[9] E. Stratakis, A. Ranella, C. Fotakis, Biomimetic micro/nanostructured functional surfaces for microfluidic and tissue engineering applications, Biomicrofluidics 5 (1) (2011) 013411. doi:10.1063/1.3553235.

[10] X. Sedao, M. V. Shugaev, C. Wu, T. Douillard, C. Esnouf, C. Maurice, S. Reynaud, F. Pigeon, F. Garrelie, L. V. Zhigilei, J.-P. Colombier, Growth Twinning and Generation of High-Frequency Surface Nanostructures in Ultrafast Laser-Induced Transient Melting and Resolidification, ACS Nano 10 (7) (2016) 6995–7007. doi:10.1021/acsnano.6b02970.

[11] X. Sedao, A. Abou Saleh, A. Rudenko, T. Douillard, C. Esnouf, S. Reynaud, C. Maurice, F. Pigeon, F. Garrelie, J.-P. Colombier, Self-Arranged

Periodic Nanovoids by Ultrafast Laser-Induced Near-Field Enhancement, ACS Photonics 5 (4) (2018) 1418–1426. doi:10.1021/acsphotonics.7b01438.

[12] J. P. Colombier, F. Garrelie, N. Faure, S. Reynaud, M. Bounhalli, E. Audouard, R. Stoian, F. Pigeon, Effects of electron-phonon coupling and electron diffusion on ripples growth on ultrafast-laser-irradiated metals, Journal of Applied Physics 111 (2012) –. doi:doi:http://dx.doi.org/10.1063/1.3676221.

[13] R. Streubel, S. Barcikowski, B. Gkce, Continuous multigram nanoparticle synthesis by high-power, high-repetition-rate ultrafast laser ablation in liquids, Optics Letters 41 (7) (2016) 1486–1489. doi:10.1364/OL.41.001486.

[14] F. Bauer, A. Michalowski, T. Kiedrowski, S. Nolte, Heat accumulation in ultra-short pulsed scanning laser ablation of metals, Optics Express 23 (2015) 1035–1043. doi:10.1364/OE.23.001035.

[15] R. Weber, T. Graf, P. Berger, V. Onuseit, M. Wiedenmann, C. Freitag, A. Feuer, Heat accumulation during pulsed laser materials processing, Optics Express 22 (9) (2014) 11312–11324. doi:10.1364/OE.22.011312.

[16] F. Di Niso, C. Gaudiuso, T. Sibillano, F. P. Mezzapesa, A. Ancona, P. M. Lugar, Influence of the Repetition Rate and Pulse Duration on the Incubation Effect in Multiple-Shots Ultrafast Laser Ablation of Steel, Physics Procedia 41 (2013) 698–707. doi:http://dx.doi.org/10.1016/j.phpro.2013.03.136.

[17] F. Di Niso, C. Gaudiuso, T. Sibillano, F. P. Mezzapesa, A. Ancona, P. M. Lugar, Role of heat accumulation on the incubation effect in multi-shot laser ablation of stainless steel at high repetition rates, Optics Express 22 (2014) 12200–12210. doi:10.1364/OE.22.012200.

[18] X. Sedao, M. Lenci, A. Rudenko, A. Pascale-Hamri, J.-P. Colombier, C. Mauclair, Additive and Substractive Surface Structuring by Femtosec-

ond Laser Induced Material Ejection and Redistribution, Materials 11 (12) (2018) 2456. doi:10.3390/ma11122456.
URL https://www.mdpi.com/1996-1944/11/12/2456

[19] J. Finger, M. Reininghaus, Effect of pulse to pulse interactions on ultrashort pulse laser drilling of steel with repetition rates up to 10 MHz, Optics Express 22 (2014) 18790–18799. doi:10.1364/OE.22.018790.

[20] B. Xia, L. Jiang, X. Li, X. Yan, Y. Lu, Mechanism and elimination of bending effect in femtosecond laser deep-hole drilling, Optics Express 23 (2015) 27853–27864. doi:10.1364/OE.23.027853.

[21] J. Schille, L. Schneider, P. Lickschat, U. Loeschner, R. Ebert, H. Exner, High-pulse repetition frequency ultrashort pulse laser processing of copper, Journal of Laser Applications 27 (S2) (2015) S28007. doi:10.2351/1.4906482.
URL https://lia.scitation.org/doi/full/10.2351/1.4906482

[22] D. Pietroy, Y. D. Maio, B. Moine, E. Baubeau, E. Audouard, Femtosecond laser volume ablation rate and threshold measurements by differential weighing, Optics Express 20 (28) (2012) 29900–29908. doi:10.1364/OE.20.029900.

[23] Y. Di Maio, J. P. Colombier, P. Cazottes, E. Audouard, Ultrafast laser ablation characteristics of PZT ceramic: Analysis methods and comparison with metals, Optics and Lasers in Engineering 50 (11) (2012) 1582–1591. doi:10.1016/j.optlaseng.2012.05.022.

[24] A. Ancona, S. Dring, C. Jauregui, F. Rser, J. Limpert, S. Nolte, A. Tnnermann, Femtosecond and picosecond laser drilling of metals at high repetition rates and average powers, Optics Letters 34 (2009) 3304–3306. doi:10.1364/OL.34.003304.

[25] I. Mingareev, A. Horn, Time-resolved investigations of plasma and melt ejections in metals by pump-probe shadowgraphy, Applied Physics A 92 (4)

(2008) 917. doi:10.1007/s00339-008-4562-7.
URL https://doi.org/10.1007/s00339-008-4562-7

[26] M. Martnez-Calderon, A. Rodriguez, A. Dias-Ponte, M. Morant-Minana, M. Gomez-Aranzadi, S. Olaizola, Femtosecond laser fabrication of highly hydrophobic stainless steel surface with hierarchical structures fabricated by combining ordered microstructures and LIPSS, Applied Surface Sciencedoi:10.1016/j.apsusc.2015.09.261.

[27] P. B. Corkum, F. Brunel, N. K. Sherman, T. Srinivasan-Rao, Thermal response of metals to ultrashort-pulse laser excitation, Physical Review Letters 61 (25) (1988) 2886.

[28] R. Fang, A. Vorobyev, C. Guo, Direct visualization of the complete evolution of femtosecond laser-induced surface structural dynamics of metals, Light: Science & Applications 6 (3) (2017) e16256.

[29] C. A. Hartmann, T. Fehr, M. Brajdic, A. Gillner, Investigation on laser micro ablation of steel using short and ultrashort ir multipulses, JLMN-Journal of Laser Micro/Nanoengineering 2 (1) (2007) 44–48.

[30] W. Zhang, G. Cheng, Q. Feng, L. Cao, Picosecond laser-induced formation of spikes in a single crystal superalloy, Applied Surface Science 258 (23) (2012) 9452–9456.

[31] K. T. Ahmmed, E. J. Y. Ling, P. Servio, A.-M. Kietzig, Introducing a new optimization tool for femtosecond laser-induced surface texturing on titanium, stainless steel, aluminum and copper, Optics and Lasers in Engineering 66 (2015) 258–268.

[32] F. Fraggelakis, G. Mincuzzi, J. Lopez, I. Manek-Hönninger, R. Kling, Texturing metal surface with mhz ultra-short laser pulses, Optics Express 25 (15) (2017) 18131–18139.

[33] P. B. Johnson, R.-W. Christy, Optical constants of the noble metals, Physical review B 6 (12) (1972) 4370.

[34] Z. Lin, L. V. Zhigilei, V. Celli, Electron-phonon coupling and electron heat capacity of metals under conditions of strong electron-phonon nonequilibrium, Physical Review B 77 (7) (2008) 075133.

[35] E. Bévillon, J.-P. Colombier, B. Dutta, R. Stoian, Ab initio nonequilibrium thermodynamic and transport properties of ultrafast laser irradiated 316l stainless steel, The Journal of Physical Chemistry C 119 (21) (2015) 11438–11446.

[36] Y. V. Petrov, K. P. Migdal, D. V. Knyazev, N. A. Inogamov, P. R. Levashov, Transport properties of copper with excited electron subsystem 774 (1) (2016) 012103.

[37] J. J. Valencia, P. N. Quested, Thermophysical properties, Modeling for Casting and Solidification Processing (2001) 189.

[38] J. Brillo, I. Egry, Surface tension of nickel, copper, iron and their binary alloys, Journal of Materials Science 40 (9-10) (2005) 2213–2216.